INSTITUT DE FRANCE
Académie des sciences

Comptes Rendus

Mécanique

Xiao-lei Hu, Jia-yi Guo, Chuan-bin Sun and Gui-gao Le

Investigation of the effect of ring-cavity on secondary-combustion and interior ballistic stabilization with low-temperature solid propellant in gas ejection

Volume 349, issue 2 (2021), p. 391-413

Published online: 5 August 2021

https://doi.org/10.5802/crmeca.92

Les Comptes Rendus. Mécanique *sont membres du Centre Mersenne pour l'édition scientifique ouverte*
www.centre-mersenne.org
e-ISSN : 1873-7234

Comptes Rendus
Mécanique
2021, 349, nº 2, p. 391-413
https://doi.org/10.5802/crmeca.92

Commentary / *Commentaire*

Investigation of the effect of ring-cavity on secondary-combustion and interior ballistic stabilization with low-temperature solid propellant in gas ejection

Xiao-lei Hu *, [a], **Jia-yi Guo** [a], **Chuan-bin Sun** [a] and **Gui-gao Le** [b]

[a] School of Mechanical Engineering, Anhui University of Technology, Ma'anshan, 243002, China

[b] School of Mechanical Engineering, Nanjing University of Science and Technology, Nanjing, 210094, China

E-mails: hu0423@126.com (X. Hu), rr861230@126.com (J. Guo), s_chuanbin@126.com (C. Sun), leguigao@mail.njust.edu.cn (G. Le)

Abstract. The potential for secondary-combustion with low-temperature solid propellant in gas generation is a potential risk to ejection application. This study performed a three-dimensional dynamic numerical simulation with Re-Normalization Group turbulence model and finite-rate/eddy-dissipation model of a two-step reaction mechanism to better understand the interaction between secondary-combustion and ring-cavity structures, and combustion effect on the loads and interior ballistic stabilization during ejection. The dynamic zone of rail cover was modelled as a rigid body, and its motion was coupled with the secondary-combustion flow in the initial chamber based on the dynamic layering method. A comparison between the numerical results and experimental data in published literature showed good agreement. Four different ring-cavity volume geometries were simulated, including no ring-cavity. Results showed that three-stage high-temperature zone can be divided in the initial chamber at the founding time in the four cases, which are a pair of spherical high-temperature zone, high-temperature zone with skirt touching walls and high-temperature zone reverse from rail cover. Additionally, increasing ring-cavity volume can accelerate the axial and radial hot gas velocity on the ring-cavity cross-section and postpone secondary-combustion process. It was also found that larger ring-cavity volume structure can smoothen the pressure and acceleration curves, reduce the out-tube-velocity and delay the out-tube-time.

Keywords. Low-temperature propellant, Secondary-combustion, Confined initial chamber, Ring-cavity, Loads, Gas ejection interior ballistic.

Manuscript received 16th June 2020, revised 28th January 2021, accepted 26th July 2021.

* Corresponding author.

1. Introduction

Low-temperature solid propellant gas ejection has attracted tremendous attention in the past two decades because of its outstanding features, which include the advantages of compacted powers, high density, small volume, more flexibility, lower cost and providing large volumes of gas in milliseconds [1,2]. Many applications of this technique can be found such as carrier-based aircraft take-off, aircraft seat ejection and other weapon launch fields [3–6]. The research on low-temperature solid propellant, whose binder is hydroxyl terminated polybutadiene (HTPB) and oxidizer is ammonium perchlorate (AP) can be traced back to the 1970s. However, due to inadequate understanding of the mechanisms of combustion of the low-temperature solid propellant, it is difficult to control the combustion and the load is sometimes over-pressure. The phenomenon of over-pressure has restricted the deployment of the low-temperature propellant in the initial chamber of gas ejection and in other applications.

Secondary-combustion is the main cause of pressure fluctuation in the initial chamber in gas ejection. Thus the physical and chemical mechanisms of low-temperature solid propellant are the necessary theoretical basis for improving the load. During the primary-combustion, because the environment is poor in oxygen and low in temperature, the combustion of low-temperature solid propellant is not complete. The primary-combustion products, containing a large amount of unburned gases, enter into the initial chamber from the gas generator and mix with fresh air to complete the combustion which is the secondary-combustion process. The combustion process not only releases a lot of heat but also produces pressure overload. A wide range of studies have been conducted on the secondary-combustion of solid propellants. The existing research shows that the physical and chemical characteristics of the compounds, combustion products of low-temperature propellant and structures of the combustion chamber have profound influence on the pressure fluctuation and combustion progress, such as spherical propellant granules [7], length of charge [8] and so on. In addition, the initial arrangement of the propellant [9], initial temperature [10], pressure [11], reaction zone thickness [12], and thermal decomposition of ammonium perchlorate [13] would affect the propellant primary-combustion process, and would further impact the pressure in secondary-combustion.

In recent years, passive control methods of combustion instability has been paid more and more attention because active control measures to suppress combustion instability involve cost and maintenance [14, 15]. Some of the most commonly used passive control components, for example, modifying the time delay [16], adding acoustic dampers [17], adding quarter-wave tubes, Helmholtz resonators [18], and shielding the fuel injectors with baffles [19] are recommended. Obstacles are placed in the combustion chamber, especially in rocket motors and confined space, to mitigate pressure instability. The obstacle configuration is chosen based on the resonant mode shapes within the rocket motor, so as to interrupt the pressure oscillations by modifying the vortex shedding. In recent years, perforated plates have been successfully used to suppress non-premixed swirl combustion instabilities under acoustic excitation [20]. The peak dynamic pressure absorption capability of plates with heterogeneously distribution holes under bias flow was evaluated, simulation and experimental results showed that plates with larger holes could reduce the pressure amplitude in the combustion chamber by approximately 70% [21, 22]. In another study, by installing a single-layer perforated plate upstream of the intake section of a lean premixed combustor, Tran *et al.* [23, 24] reduced the low-amplitude pressure fluctuations. Scarpato *et al.* [25] also found that the back-cavity of the perforated plates could suppress non-premixed swirl combustion instabilities.

Most of the previous studies have considered the passive control of combustion instability in the premixed combustor. Particularly, few researches are presented on passive control of non-premixed combustion by modification in confined combustion chamber. Attracted by this

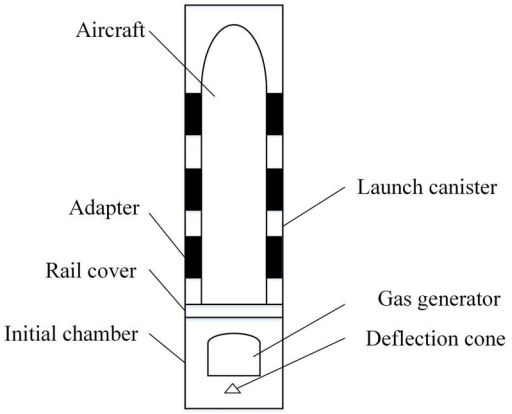

Figure 1. Structure of ejection system.

interesting structure in controlling the combustion instability, we promote a ring-cavity obstacle for low-temperature solid propellant combustion in confined space to investigate its influence on secondary-combustion and additionally the effect on the pressure load and interior ballistic stabilization during ejection. The objective of this study is to extend the understanding of specific physical mechanisms which contribute to the process of secondary-combustion high-temperature zone propagation by adding ring-cavity in confined initial chamber. The effects of low-temperature propellant, considering of $H_2/CO–O_2$ mixtures in various structures, are covered by numerical simulation of Semi-Implicit Method for Pressure-Linked Equations Couple (SIMPLEC) algorithms [26]. For the SIMPLEC algorithms, one of the limitations is that the new velocities and corresponding fluxes do not satisfy the momentum balance after the pressure correction equation is solved. However, SIMPLEC can be used in the low-Mach number compressible flow by multiple solves of the momentum predictors and the pressure correctors per time step until the residuals of all variables reduce to a desirable value [27]. In our research, experimental data in published literature is compared with and a parametric study is conducted in order to find out the relationships between secondary-combustion and ring-cavity volumes.

Our paper is structured as follows: the detailed description of confined initial chamber structure and its working process are given in Section 2. Section 3 pertains to the modelling and analysis method of secondary-combustion. In Section 4, we first show the validation of no ring-cavity initial chamber with experimental data, then we make a particular discussion on the ring-cavity volume effect on the pressure and temperature loads, species in the initial chamber and interior ballistic variations. Conclusions are presented in Section 5.

2. Ejection system description

The structure of gas ejection is illustrated in Figure 1. Paired adaptors, which are set between aircraft and canister, are used to protect the aircraft wall. The aircraft sits on the rail cover during the ejection process. Launch canister is split into two parts by rail cover, which are launch canister upside and initial chamber downside, respectively. Figure 2 is a schematic cross-section drawing of the initial chamber with no ring-cavity. Gas generation is set at the internal centre of the initial chamber. The deflection cone is set under the nozzle outlet of gas generation. Ejection working process begins from the low-temperature propellant primary-combustion in the gas generator. While the jet flows feed into the initial chamber through the nozzle, they meet the cone deflection

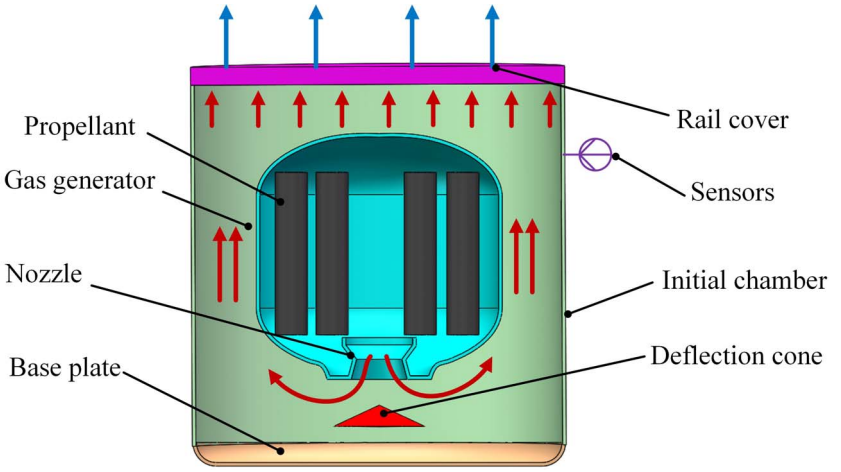

Figure 2. Cross-section of no ring-cavity initial chamber.

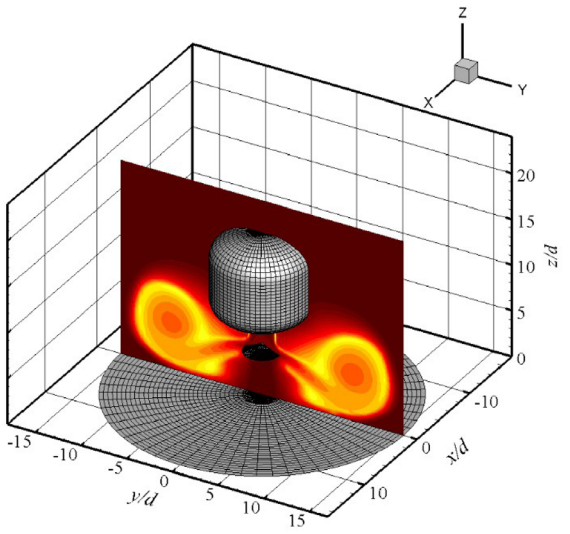

Figure 3. Flow configuration with no ring-cavity.

and separate. Part of it passes through the cone deflection and hide under it. Most of the jet flows go up and promote the upward movement of the rail cover. The volume of initial chamber increases during ejection. While jet flows exhausted from the gas generator meet the fresh air in the initial chamber, the secondary-combustion phenomenon could be triggered.

3. Simulation and analysis methods

3.1. *Physical models*

The flow configuration, structure meshes and coordinate system in the present research are shown in Figure 3. The nozzle is located on $z = 8.5d$ from the base plate. d is the throat diameter, which is 68 mm. The diameter of the initial chamber is $15d$, and height is $19d$. The deflection

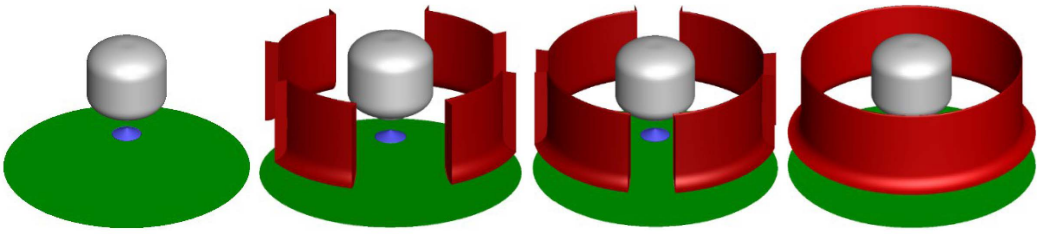

(a) no ring-cavity (b) volume of 0.24 m^3 (c) volume of 0.36m^3 (d) volume of 0.48 m^3

Figure 4. Structures of four different ring-cavities.

cone is located on $z = 4.8d$ with 130° angle of cone. We consider four different ring-cavity structures, whose volumes are zero, 0.24 m^3, 0.36 m^3 and 0.48 m^3, as shown in Figures 4(a)–(d). Considering the complexity of the system, the ejection process is analysed based on the following assumptions:

(1) The system is perfectly sealed regardless of gas leakage during the entire period.
(2) The grain burns completely, and all combustion products are in the gas phase.
(3) The mechanical parts of initial chamber are in excellent physical and mechanical states regardless of gas ablation on the wall.

3.2. *Governing equation*

A three-dimensional finite-volume model is established to analyse the secondary-combustion process in the initial chamber. The governing equation for mass, momentum and energy of the initial chamber fluid regions are as follows:

$$\frac{\partial}{\partial t}(\rho_m) + \nabla \cdot (\rho_m \vec{v}_m) = 0 \tag{1}$$

$$\frac{\partial}{\partial t}(\rho_m \vec{v}_m) + \nabla \cdot (\rho_m \vec{v}_m \vec{v}_m) = -\nabla p + \nabla \cdot [\mu_m (\nabla \vec{v}_m + \vec{v}_m^T)] + \rho_m \vec{g} + \vec{F} \tag{2}$$

$$\frac{\partial}{\partial t}\sum_i \alpha_i \rho_i h_i + \nabla \cdot \sum_i (\alpha_i \vec{v}_i (\rho_i h_i + p)) = \nabla \cdot \left(-\sum_i h_i \vec{J}_i \right) \tag{3}$$

where $\vec{v}_m$ is the multi-species averaged velocity in initial chamber, $\vec{F}$ is body force of multi-species, α_i is the ith species mass fraction, h_i is the ith species enthalpy, $\vec{J}_i$ is the ith species diffusive flux. For other parameters related to (1)–(3) refer to [28].

The conservation equation is

$$\frac{\partial}{\partial t}(\rho Y_i) + \nabla \cdot (\rho \vec{v} Y_i) = -\nabla \cdot \vec{J}_i + R_i + S_i \tag{4}$$

where R_i is the net rate of production of species i by chemical reaction and S_i is the rate of creation by adding from the dispersed phase. The equation of this form will be solved for $N-1$ species where N is the total number of fluid phase chemical species present in the system. $\vec{J}_i$ is the diffusion flux of species i, which arises due to gradients of concentration and temperature. In our case, we use Fick's law to model mass diffusion due to concentration gradients, under which the diffusion flux can be written as

$$\vec{J}_i = -\rho \left(D_{i,m} + \frac{\mu_t}{Sc_t} \right) \nabla Y_i - D_{T,i} \frac{\nabla T}{T} \tag{5}$$

where $D_{i,m}$ is the mass diffusion coefficient for species i in the mixture, and $D_{T,i}$ is the thermal diffusion coefficient, Sc_t is the turbulent Schmidt number, $Sc_t = \mu_t/\rho D_t$, μ_t is the turbulent viscosity, D_t is the turbulent diffusivity. In this study, the value of Sc_t is 0.7.

3.3. *Finite-rate/eddy-dissipation model*

Consider the rth reaction written in general form as follows:

$$\sum_{i=1}^{N} v'_{i,r} M_i \underset{k_r}{\overset{k_r}{\rightleftharpoons}} \sum_{i=1}^{N} v''_{i,r} M_i \tag{6}$$

where N is the number of chemical species in the system, $v'_{i,r}$ is the stoichiometric coefficient for reactant i in reaction r, $v''_{i,r}$ is the stoichiometric coefficient for product i in reaction r, k_r is the rate constant for reaction r.

The molar rate of creation/destruction of species i in reaction r is given by

$$\widehat{R}_{i,r} = \Gamma(v''_{i,r} - v'_{i,r}) \left(k_{f,r} \prod_{j=1}^{N} [c_{j,r}]^{\eta'_{j,r}} - k_{b,r} \prod_{j=1}^{N} [c_{j,r}]^{\eta''_{j,r}} \right) \tag{7}$$

where $c_{j,r}$ is molar concentration of species j in reaction r (kmol/m^3), $\eta'_{j,r}$ is the rate exponent for reactant species j in reaction r, $\eta''_{j,r}$ is the rate exponent for product species j in reaction r.

The rate constant for reaction r, k_r is computed using the Arrhenius expression

$$k_r = AT^{T_a} \mathrm{e}^{-N/RT} \tag{8}$$

where A is pre-exponential factor, T_a is the temperature exponent, N is the activation energy for the reaction, R is universal gas constant.

For the eddy-dissipation model, the net rate of production of species i due to reaction r, $R_{i,r}$ is given by the smaller of the two expressions below:

$$R_{i,r} = (v''_{i,r} - v'_{i,r}) M_{w,i} A \rho \frac{\varepsilon}{k} \min_R \left(\frac{Y_R}{v'_{R,r} M_{w,R}} \right) \tag{9}$$

$$R_{i,r} = (v''_{i,r} - v'_{i,r}) M_{w,i} AB \rho \frac{\varepsilon}{k} \frac{\sum_P Y_P}{v''_{j,r} M_{w,j}} \tag{10}$$

where Y_P is the mass fraction of any product species P, Y_R is the mass fraction of a particular reactant R, A is an empirical constant equal to 4.0, B is an empirical constant equal to 0.5.

The chemical reaction rate is governed by the large-eddy mixing time scale, k/ε, combustion proceeds whenever turbulence is present, $k/\varepsilon > 0$, both the finite-rate reaction rates (7) and eddy-dissipation (9) and (10) rates are calculated. The reaction rate is taken as the minimum of these two rates. In practice, the finite-rate kinetics act as kinetic "switch", preventing reaction. Once the reaction is ignited, the eddy-dissipation rate is generally smaller than the Arrhenius rate, the reactions are mixing-limited.

3.4. *Turbulence model*

Re-Normalization Group turbulence model [29] is adopted to simulate the small scale motion, the rapidly strained swirling flows in the initial chamber. The transport equations for Re-Normalization Group turbulence model are expressed as follows

$$\frac{\partial \rho_m k}{\partial t} + \frac{\partial \rho_m u_i k}{\partial x_i} = \frac{\partial}{\partial x_i} \left[\left(\mu + \frac{\mu_t}{\sigma_k} \right) \frac{\partial k}{\partial x_i} \right] + P_k - \rho_m \varepsilon \tag{11}$$

$$\frac{\partial \rho_m \varepsilon}{\partial t} + \frac{\partial \rho_m u_i \varepsilon}{\partial x_i} = \frac{\partial}{\partial x_i} \left[\left(\mu + \frac{\mu_t}{\sigma_\varepsilon} \right) \frac{\partial \varepsilon}{\partial x_i} \right] + \frac{\varepsilon}{k} (C_{1\varepsilon} P_k - C^*_{2\varepsilon} \rho_m \varepsilon) \tag{12}$$

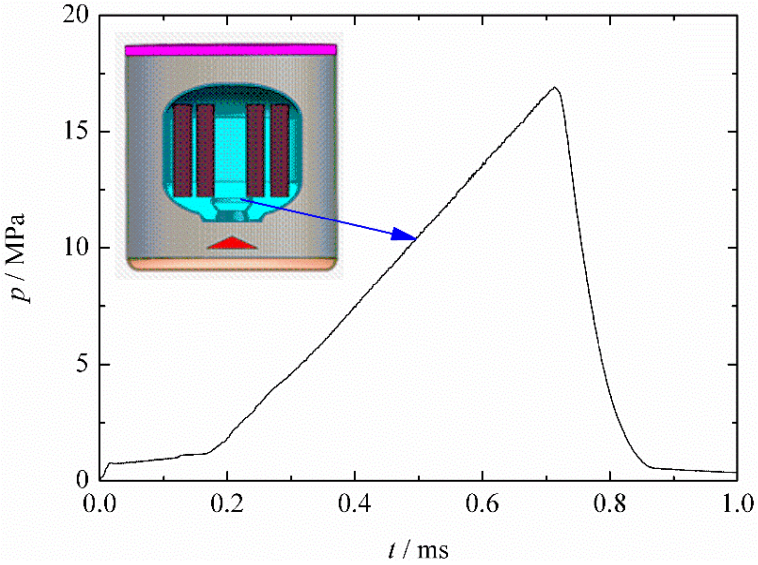

Figure 5. Pressure variation of nozzle inlet.

Table 1. Species and mass fractions of nozzle inlet

Species	H_2O	CO	H_2	CO_2	N_2	HCl
Mass fraction	0.004	0.564	0.05	0.002	0.26	0.12

3.5. *Boundary condition and simulation models*

Based on the working condition in the confined space, a no-slip wall which indicates that the fluid sticks to the wall, is applied to all the wall boundaries in the initial chamber. The material of the initial chamber, gas generator, deflection cone and ring-cavities is steel. Rail cover wall will move upwards while the pressure in the initial chamber is increased enough to promote the movement of the aircraft. Pressure inlet is used for the nozzle inlet boundary of gas generator. The nozzle inlet pressure variation with time is shown in Figure 5. The temperature of the nozzle inlet is 1500 K within 50 ms after the low-temperature solid propellant combustion, this is coupled into Fluent by UDF at each time step. The mass fractions of nozzle inlet species are listed in Table 1, computed by CEA software, which are used to calculate chemical equilibrium product concentrations from the reactants and determine the thermodynamic and transport properties for product mixture [30]. The initial air pressure in initial chamber is 0.101 MPa, and the temperature is 300 K. The mass fractions of N_2 and O_2 in the initial chamber are 0.77 and 0.23, respectively. In this research, finite-rate/eddy-dissipation model, which is intensely coupled with turbulent flow, is used to calculate the secondary-combustion reaction rate in the initial chamber. Two-step hydrogen-air and carbon monoxide-air chemical models are used to simulate the secondary-combustion. Combustion mechanisms and rate parameters are shown in Table 2.

3.6. *Dynamic layering method*

In this section, we present the dynamic layering method which is used to simulate the rail cover movement. The principle of the method is shown in Figure 6. While the initial chamber is expanding during ejection, the mesh cell height is enlarged. To ensure the accuracy of the

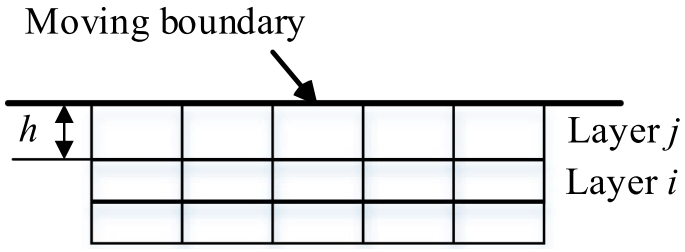

Figure 6. Mesh movement of dynamic layering method.

Table 2. Rate parameters for secondary-combustion mechanism

Step	Reaction	A (m, kg, mol, s, K)	N	T_a (K)
1	$2CO + O_2 = 2CO_2 + M$	2.24×10^{12}	1.7×10^8	0
2	$2H_2 + O_2 = 2H_2O$	9.87×10^8	3.1×10^7	0

Note: [M] = $0.5H_2O$.

simulation, the cell layer of grid closed to the moving boundary is split into two new units with the adjacent layer *j* based on the unit height of boundary layer *i*.

As shown in Figure 6, while the cells in layer *j* are expanding, the cell heights are allowed to increase until

$$h_{\min} > (1 + \alpha_s) h_{\text{ideal}} \tag{13}$$

where $h_{\min}$ is the minimum cell height of cell layer *j*, h_{ideal} is the ideal cell height, and α_s is the layer split factor. In our case, we defined the $h_{\text{ideal}} = 0.005$ m and $\alpha_s = 0.4$.

3.7. *Calculation method*

The simulation of secondary-combustion in initial chamber is stated by solving mass, momentum and energy equation. The governing equations are solved by commercial software package Fluent. SIMPLEC algorithm is chosen to solve the pressure-velocity coupled equation. The convective term and diffusion term are computed by a second-order upwind scheme and central difference scheme, respectively.

4. Results and discussion

4.1. *Validation*

To validate the numerical simulation method, we compared our three-dimensional no ring-cavity model with experimental data in published literature [31, 32]. Figures 7(a) and (b) are comparisons of monitoring pressure and temperature curves with experimental data [31, 32]. As shown in Figure 2, the monitoring point is set as the literature illustration, which is one fifth under the rail cover. The *p*–*t* curves in Figure 7(a) show that the increase in simulation pressure is consistent with the experimental results, both of which climb from zero to 0.89 MPa in 0.15 s, and then goes down. After that, the pressure curves climb again and attain the second pressure peak at approximately 0.7 s. Figure 7(b) compares the temperature curves with the experimental results. The plots show that simulation results are consistent with experimental data. Both climb first, before going down. Although there are some differences in pressure and temperature plots compared to the experimental results, the key features of the pressure and temperature loads

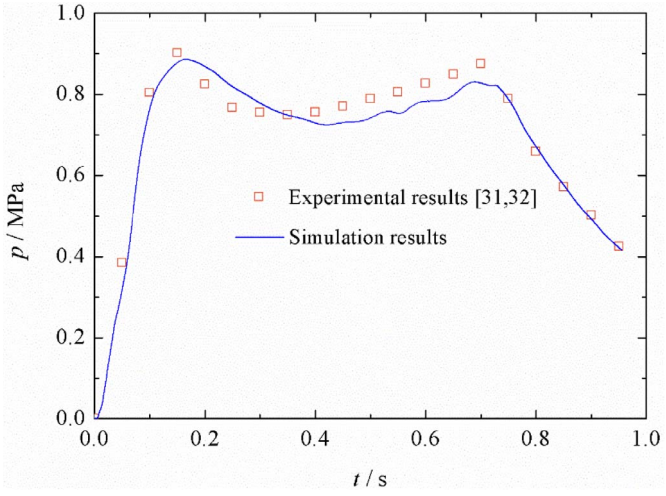

(a) Pressure comparison

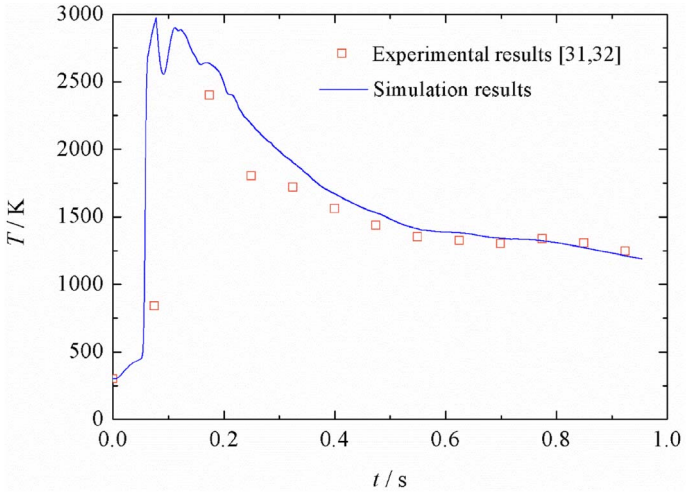

(b) Temperature comparison

Figure 7. Comparisons of monitoring point pressure and temperature curves with experimental data [31,32].

in the experiment are reproduced by the simulation. In particular, the double pressure peak phenomenon is reproduced in Figure 7(a).

4.2. *Development of secondary-combustion fluid fields*

We are interested in the ring-cavity structures on the secondary-combustion in the initial chamber. To study this, we considered four different ring-cavity geometric variations consisting of the same basic initial chamber, but with differently shaped ring-cavities (Figure 4). In the following sections we describe the configurations of fluid zone and present the associated relationship.

To study the ring-cavity influence on the velocity fields, we choose the case of 0.24 m^3 ring-cavity as a representative. Figures 8 and 9 are the cross-section velocity fields with 0.24 m^3 ring-cavity. From the velocity fields, we can see that the gas velocity is reduced by the expansion from

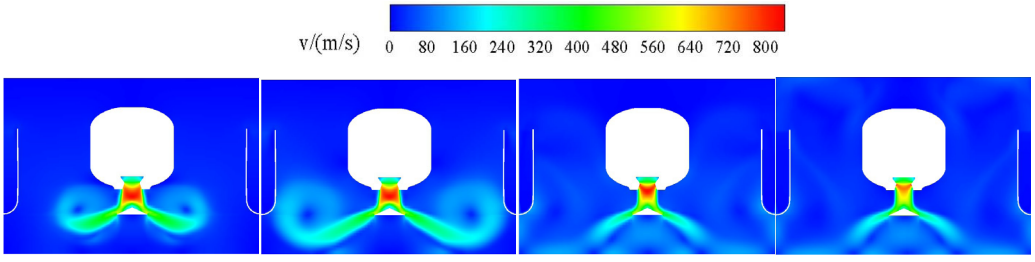

Figure 8. Sequence of instantaneous velocity fields showing the numerical secondary-combustion propagating with 0.24 m^3 ring-cavity on YOZ cross-sections.

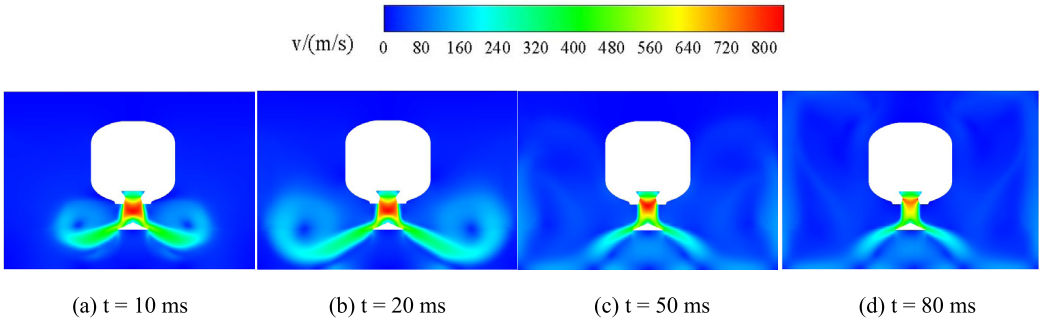

Figure 9. Sequence of instantaneous velocity fields showing the numerical secondary-combustion propagating with 0.24 m^3 ring-cavity on cross-section rotating 5° from YOZ plane.

the nozzle. In Figures 8 and 9, most of the initial chamber are subsonic except the outlet of the nozzle. The ring-cavity changed the flow pattern. With ring-cavity cross-section, the gas flows along the wall of the ring-cavity, whereas gas flows along the wall of tube without ring-cavity.

Previous research [31, 32] suggested that secondary-combustion activity occurs in the first 0.2 s. Before the high-temperature zone surrounding gas generator, combustion is most intense than at any other time during ejection. So we choose the fluid sequence at the founding time to analyse the ring-cavity structure's influence on the secondary-combustion, load and interior ballistic stabilization.

Figures 10(a)–(d) are a sequence of instantaneous oxygen fields without ring-cavity on YOZ cross-sections. From the cross-section, we can see that oxygen consumption is initially along the cone wall, and then along the tube wall.

Figures 11(a)–(d) are a sequence of instantaneous streamlines and temperature fields showing the numerical secondary-combustion gas propagating without ring-cavity on YOZ cross-sections. In this no ring-cavity configuration, the secondary-combustion flow propagation can be discussed in terms of three stages: (1) a pair of spherical high-temperature zone, (2) high temperature with skirt touching side walls, (3) high-temperature reverse from rail cover. Some of these stages are similar to premixed combustion studies [33, 34]. Before discussing each of the three stages, we comment briefly on the jet flow behaviour as shown in the temperature maps. During the primary-combustion in gas generator, the combustion of low-temperature propellant is incomplete due to the oxygen-poor environment and low temperature. After the primary-combustion, jet flows with incomplete combustion products are squeezed out from the gas

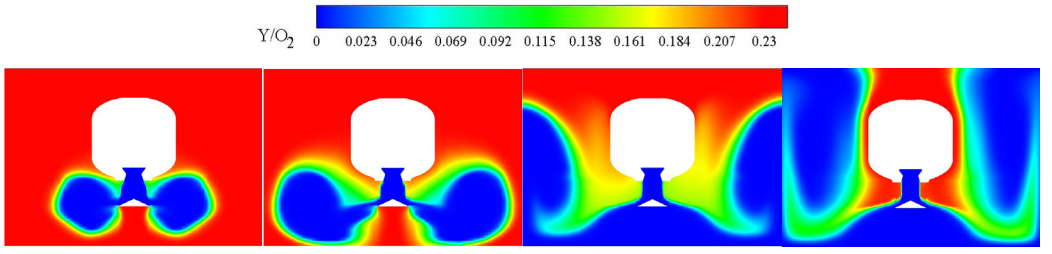

Figure 10. Sequence of instantaneous oxygen fields showing the numerical secondary-combustion propagating with no ring-cavity on YOZ cross-sections.

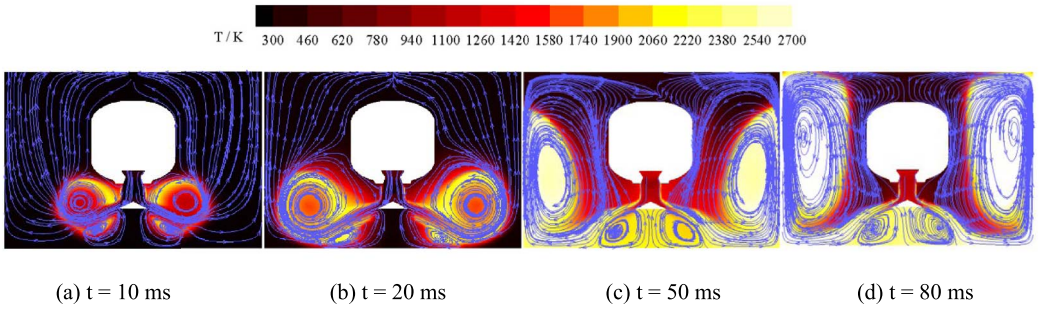

Figure 11. Sequence of instantaneous streamlines and temperature fields showing the numerical secondary-combustion propagating with no ring-cavity on YOZ cross-sections.

generation and mixed with fresh air in the initial chamber to complete the combustion process, which releases lots of energy and results in the temperature increasing. Due to limited oxygen content in the confined initial chamber, the secondary-combustion process will end when oxygen is exhausted. In Figures 9(a)–(d), jet flows from the gas generator nozzle meet the deflection cone and then are separated into two branches. Most of the jet flows go down along the conical surface and expand in the initial chamber. The other jets cross over the deflection cone and gather under it. As the low-temperature propellant continues burning, more and more jet flows go into the initial chamber. The jet flows feed into the confined initial chamber space.

As shown in the no ring-cavity case in Figures 9(a)–(b), the secondary-combustion high-temperature zone propagated in the initial chamber develops into a pair of spherical high-temperature zone, which expands at $t = 20$ ms, and begin to evolve into hot gas with their skirt touching the side walls at $t = 50$ ms. In the first stage, the hot gases expand outwards, restricted by the deflection cone, without any effect of the ring-cavity. Spherical high-temperature zone development in the confined space can also be found in a narrow tube flame acceleration with premixed combustion [33]. However, in our study, there are two spherical shapes which are asymmetrically distributed. Additionally, each of the spherical hot gas contains two reverse vortices influenced by the deflection cone surface. Taking the left hand side for example, the bigger vortex is higher than the deflection cone, and the other is under it. As pressure increases, burned gases expand and the bigger vortex is enlarged by gas expansion at $t = 50$ ms. Meanwhile the bigger vortex core has little change. The smaller vortex core is extruded lower and approaches the base plate, influenced by the bigger vortex expansion.

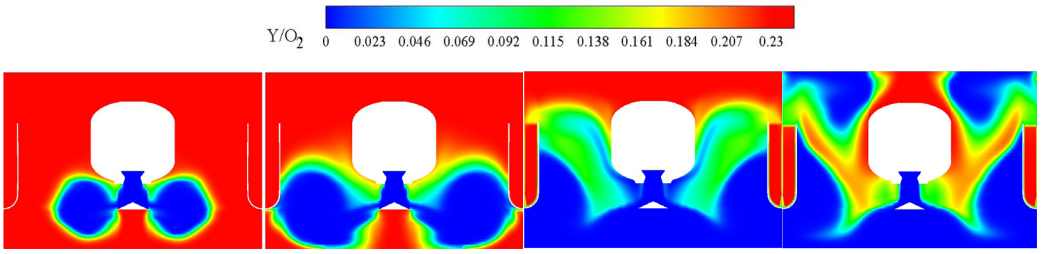

Figure 12. Sequence of instantaneous oxygen fields showing the numerical secondary-combustion propagating with ring-cavity volume of 0.24 m^3 on YOZ cross-section.

As stated in [34], the high-temperature zone skirt refers to the secondary-combustion high-temperature zone front moving towards the wall. In stage (2) shown in Figure 9(c), high-temperature zone with skirt touching side walls, the secondary-combustion high-temperature zone is significantly elongated along the initial chamber side walls, which is the same as in narrow long tube high-temperature zone acceleration [35]. As the pressure of low-temperature propellant increases, jet flows stretch the high-temperature zone in the initial chamber. The secondary-combustion high-temperature zone near the initial chamber wall are inclined to the chamber axis and makes an acute angle with the wall due to the sidewall effects, as shown in $t = 50$ ms. Restricted by the sidewall, the bigger flow vortex is not only closed to the initial chamber wall but also raised to the vortex core compared with $t = 20$ ms.

The secondary-combustion high-temperature zone is reversed from the rail cover and forms a moustache-shaped high-temperature zone at $t = 80$ ms which is stage (3). Once the high-temperature zone reaches the rail cover, the high-temperature zone suddenly changes expansion direction due to the restriction of area. The high-temperature zone is mainly propagated from axial expansion to radial expansion. A moustache-shaped unburned area is formed and high-temperature zone moves towards the gas generator, as shown in Figure 9(d). Taking the left hand side for example, the bigger vortex core is raised and extruded close to the initial chamber wall, while the smaller vortex still stays under the deflection cone. The temperature maps also show a noticeable shear layer which is formed along the extension cord of the deflection cone. This can explain why a temperature gradient exists between the two vortices.

Figures 12 and 13 are a sequence of instantaneous oxygen fields with ring-cavity volume of 0.24 m^3 on YOZ cross-sections and rotating plane. From the oxygen fields of cross-section in Figures 12(a)–(d), we can see that the ring-cavity cross-section can store oxygen compared with no ring-cavity cross-section in Figures 13(a)–(d) during ejection.

Figures 14 and 15 are the sequences of instantaneous streamlines and temperature fields showing the numerical secondary-combustion high-temperature zone propagating with ring-cavity volume of 0.24 m^3 on XOY cross-section and 5° rotating cross-section from the YOZ plane, respectively. From these two cross-sections in the initial chamber with ring-cavities, we can see that the temperature fields and flow patterns have little difference at $t = 80$ ms.

On the YOZ cross-section in Figure 14, there are also three-stage high-temperature zones in the initial chamber: a pair of spherical high-temperature zone, high-temperature zone with skirt touching walls and high-temperature zone reverse of rail cover. At $t = 10$ ms and $t = 20$ ms, with the low-temperature propellant combustion, the burned jet flows expand in the initial chamber and form a pair of spherical high-temperature zone. There are two pairs of vortices which distribute on both sides of the deflection cone. Take the left hand side for example, the vortex core

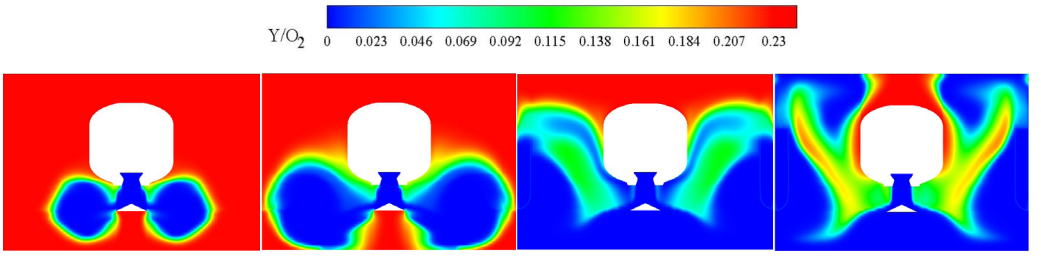

(a) t = 10 ms (b) t = 20 ms (c) t = 50 ms (d) t = 80 ms

Figure 13. Sequence of instantaneous oxygen fields showing the numerical secondary-combustion propagating with ring-cavity volume of 0.24 m^3 on cross-section rotating 5° from YOZ plane.

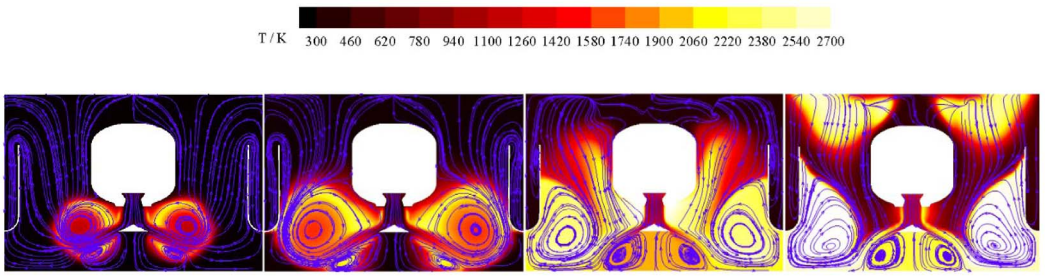

(a) t = 10 ms (b) t = 20 ms (c) t = 50 ms (d) t = 80 ms

Figure 14. Sequence of instantaneous streamlines and temperature fields showing the numerical secondary-combustion propagating with ring-cavity volume of 0.24 m^3 on YOZ cross-section.

location is the same as the no ring-cavity case at $t = 10$ ms and $t = 20$ ms in Figures 11(a) and (b). In particular, an important feature of this flow streamline is that the burned gas not only goes up into the unburned region, but also is propagated into the ring-cavity, as shown in Figures 14(a) and (b). While the jet flows from the gas generator increased, the flows touch the initial chamber wall and gas generator wall at $t = 50$ ms, which is different from the no ring-cavity case in Figure 11(c). The flow streamline patterns tend to be concave near the ring-cavity wall downside. This behaviour can promote the high-temperature zone to be more close to the gas generator. From the streamlines near the gas generator at $t = 50$ ms, we can see that the high-temperature zone near the gas generator comes from the rebounding gases of rail cover, and not from rebounding flows of the ring-cavity wall. This will be discussed in the following. Additionally, there are small vortices at the entrance of the ring-cavity at $t = 50$ ms, which disappear at $t = 80$ ms. This may be caused by the enhanced reverse flow from the rail cover.

On the other hand, the flow developments on no ring-cavity cross-section rotating 5° from YOZ plane in Figure 11 are different from the ring-cavity cross plane in Figure 14. On no ring-cavity cross-section in Figures 15(a) and (b), the temperature maps and streamlines are the same as ring-cavity cross plane in Figure 14 at $t = 10$ ms and $t = 20$ ms. There is also a pair of spherical high-temperature zone which distributes on both sides of deflection cone. At $t = 50$ ms, burned gases have surrounded the gas generator downside in Figure 15(c), while there is a temperature gradient near the gas generator in Figure 10(c). From the comparison between Figures 14(c)

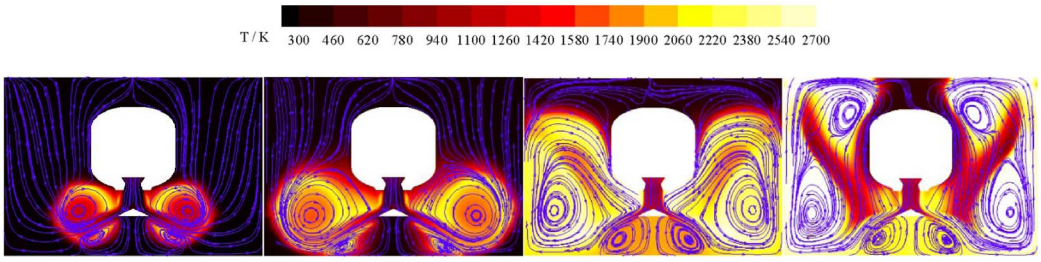

Figure 15. Sequence of instantaneous streamlines and temperature fields showing the numerical secondary-combustion propagating with ring-cavity volume of 0.24 m^3 on cross-section rotating 5° from YOZ plane.

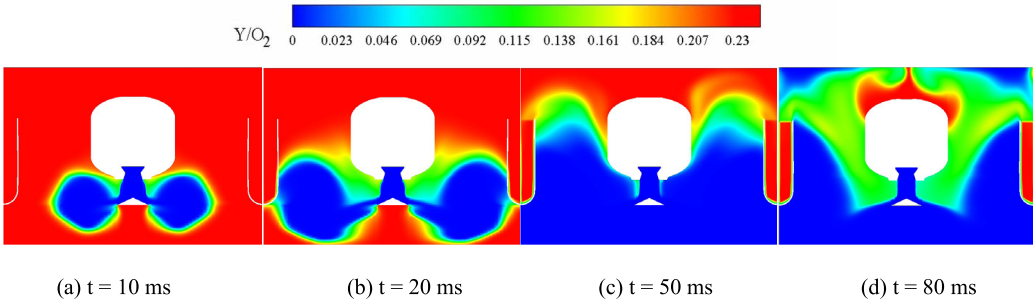

Figure 16. Sequence of instantaneous oxygen fields showing the numerical secondary-combustion propagating with ring-cavity volume of 0.36 m^3 on YOZ cross-section.

and 15(c), it can be deduced that: (1) burned gases in ring-cavity plane propagate faster than no ring-cavity plane due to the blockage of obstructions; (2) gases surrounding the gas generator in Figure 14(c) is extruded by burned gas near gas generator in Figure 11(c), which causes a temperature gradient in Figure 13(c). Compared with no ring-cavity case in Figure 11(c), the secondary-combustion high-temperature zone encircles the gas generator in the lower side in Figure 15(c), while there is a temperature gap in no ring-cavity case in Figure 11(c). It could be concluded that the ring-cavity can accelerate the secondary-combustion axial and radial flow on the ring-cavity cross-section. At $t = 80$ ms in Figure 15(d), the high-temperature zone flows along the initial chamber wall and gets to the rail cover wall. Restricted by the region wall, the burned gases form reverse jet flows and a new pair of vortices form on both sides of the gas generation head. In particular, an important feature of this reversed flow is that it contains not only hot burned gases, but also the cold fresh unburned air. This phenomenon is similar to the results by Kurdyumov [36] and Xiao Huahua [34] in channel flame dynamics. This flow behaviour creates the temperature gradient between the bigger vortex near the ring-cavity and the new vortex at the head of the gas generator. It can also be shown that although there is no real relation between the hot gas near the ring-cavity and under rail cover, the hot gas reverses from the rail cover in Figure 14(d).

Figures 16 and 17 are a sequence of instantaneous oxygen fields with ring-cavity volume of 0.36 m^3 on YOZ cross-sections and rotating plane. From the oxygen fields of cross-section in Figures 16(a)–(d), we can also see that the ring-cavity cross-section can store oxygen compared to no-ring-cavity cross-section in Figures 17(a)–(d).

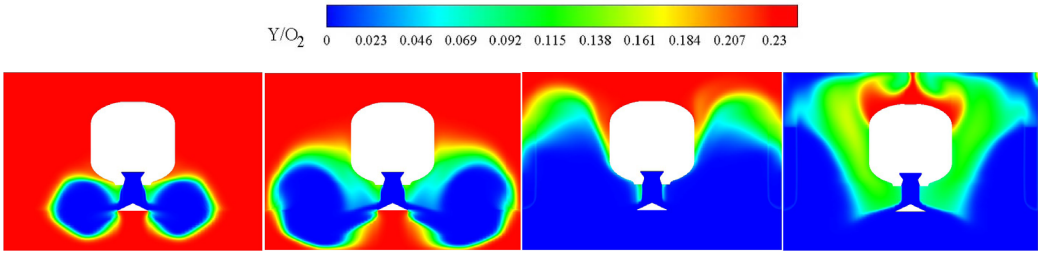

(a) t = 10 ms (b) t = 20 ms (c) t = 50 ms (d) t = 80 ms

Figure 17. Sequence of instantaneous oxygen fields showing the numerical secondary-combustion propagating with ring-cavity volume of 0.36 m^3 on cross-section rotating 5° from YOZ plane.

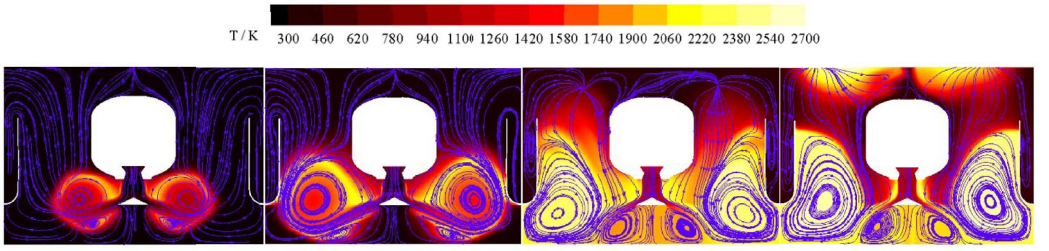

(a) t = 10 ms (b) t = 20 ms (c) t = 50 ms (d) t = 80 ms

Figure 18. Sequence of instantaneous streamlines and temperature fields showing the numerical secondary-combustion propagating with ring-cavity volume of 0.36 m^3 on YOZ cross-sections.

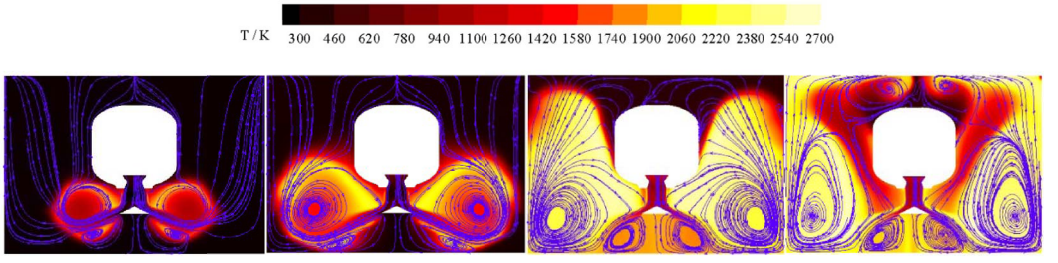

(a) t = 10 ms (b) t = 20 ms (c) t = 50 ms (d) t = 80 ms

Figure 19. Sequence of instantaneous streamlines and temperature fields showing the numerical secondary-combustion propagating with ring-cavity volume of 0.36 m^3 on a cross-sections rotating −5° from YOZ plane.

Figures 18 and 19 are sequences of instantaneous streamlines and temperature fields showing the numerical secondary-combustion propagating with ring-cavity volume of 0.36 m^3 on XOY cross-section and −5° rotating from YOZ plane. From these two cross-sections with ring-cavity in initial chamber, we can see that the temperature fields and flow patterns are similar as in the case with ring-cavity volume of 0.24 m^3. There are also three stages of high-temperature zone propagation, a pair of spherical high-temperature zone, high-temperature zone with skirt

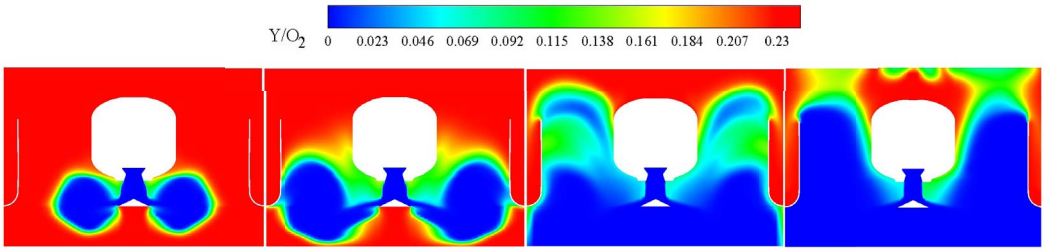

Figure 20. Sequence of instantaneous oxygen fields showing the numerical secondary-combustion propagating with ring-cavity volume of 0.48 m^3 on YOZ cross-section.

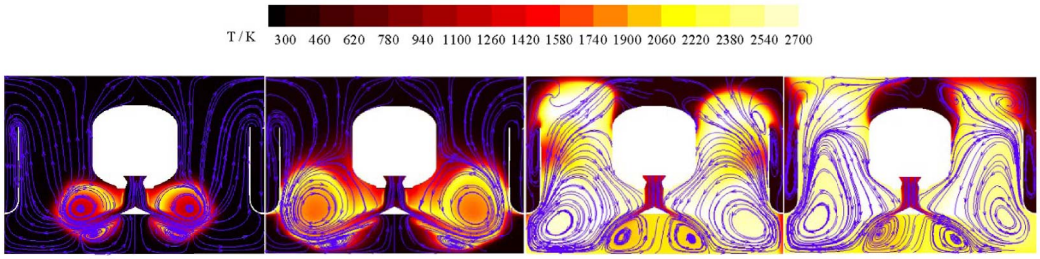

Figure 21. Sequence of instantaneous streamlines and temperature fields showing the numerical secondary-combustion propagating with ring-cavity volume of 0.48 m^3 on YOZ cross-sections.

touching walls and high-temperature zone reverses from rail cover. On the first stage at t = 10 ms and t = 20 ms in Figures 18(a) and (b), there are a pair of spherical high-temperature zones and the flow patterns are the same as that of the ring-cavity volume of 0.24 m^3 case. At t = 50 ms, although the streamlines and temperature maps are similar to the 0.24 m^3 ring-cavity case, the high-temperature zone height of 0.36 m^3 case is lower. At t = 80 ms, the extend of high-temperature zone reverses from rail cover are less than 0.24 m^3 case. Influenced by the reversed flows, the vortex cores at the headside of the gas generator are higher than 0.24 m^3 case. It can be concluded that larger ring-cavity volume can accelerate the secondary-combustion axial propagation.

Figures 20(a)–(d) are a sequence of instantaneous oxygen fields and temperature fields with ring-cavity volume of 0.48 m^3 on YOZ cross-sections. We also can see that the ring-cavity cross-section can store oxygen compared to no-ring-cavity case in Figures 10(a)–(d). The oxygen consumption process will be discussed in the following.

Figures 21(a)–(d) show a sequence of instantaneous streamlines and temperature fields generated as the secondary-combustion develops with ring-cavity volume of 0.48 m^3 on a YOZ cross-section. In this ring-cavity volume of 0.48 m^3 configuration, the secondary-combustion flow propagated can also be discussed in terms of three stages: a pair of spherical high-temperature zone, high-temperature zone with its skirt touching walls and high-temperature zone reverses from rail cover. On the first stage at 10 ms and 20 ms in Figures 21(a) and (b), there are a pair of spherical high-temperature zones and the flow pattern is the same as the ring-cavity volume of 0.24 m^3 and volume of 0.36 m^3. In addition, the secondary-combustion high-temperature zone

radial velocity of 0.48 m^3 case is the fastest in the four structures. The secondary-combustion high-temperature zone front has nearly got the rail cover wall at $t = 50$ ms in Figure 21(c), while there is a short distance between the high-temperature zone front and rail cover in the other three cases. In Figure 21(d), the secondary-combustion high-temperature zone almost embraces the gas generator.

We can conclude from the above results that there are three stages of secondary-combustion high-temperature zone, and the second and third stages are relatively insensitive to the ring-cavity volume. Larger ring-cavity volume can change the high-temperature zone structure between gas generator and initial chamber wall. Additionally, increasing volume can accelerate the axial and radial secondary-combustion velocity on the ring-cavity cross-section. However, the ring-cavity volume has little influence to the combustion and vortex structure under the deflection cone.

4.3. *Discussion of load and species variation in initial chamber*

To make a deep analysis on the ring-cavity effect on the load and interior trajectory, we discussed the load, species, and interior ballistic variations during ejection. Figures 22(a) and (b) are pressure and temperature load comparison of four different ring-cavity structures in the initial chamber. From the pressure load curves, we can see that as the ring-cavity volume increasing, the two pressure peaks fade away. In the four cases, volume of 0.48 m^3 ring-cavity case has the smoothest pressure curve.

In the no ring-cavity case in Figure 22(a), the first pressure is 0.9 MPa at $t = 0.18$ s; while the case with ring-cavity volume of 0.48 m^3 is 0.78 MPa at $t = 0.3$ s. This trend can be concluded according to the pressure plots, that the first pressure peak is decreasing and the first peak time is delayed. This tendency is also applicable to the secondary pressure peak while the ring-cavity volume changes from 0 to 0.36 m^3. However, the secondary pressure peak is not reduced in the 0.48 m^3 case compared to 0.36 m^3. Another difference with the first pressure peak variation is that the time of secondary pressure peak is maintained at 0.76 s in the four cases. Additionally, the first and secondary pressure peak in Figure 22(a) can be expressed by

$$p_1 = 0.87994 - 0.16738x (0 \le x \le 0.48) \tag{14}$$

$$p_2 = 0.82974 - 0.57223x + 1.09691x^2 (0 \le x \le 0.48) \tag{15}$$

while p_1 (MPa) is the first pressure peak, p_2 (MPa) is the secondary pressure peak, x (m^3) is volume of ring-cavity.

In the temperature curves in Figure 22(b), we can see that the temperature peak is unchanged in the four ring-cavity cases. The maximum temperature is 2900 K. But the time of temperature peak is delayed with increase in ring-cavity volume.

Compared to loads of four ring-cavity cases, there are clear pressure and temperature distinctions between the cases with no ring-cavity and ring-cavity cases. The load plots show that ring-cavity structure can have an effect on the pressure peak and the temperature peak time. These differences can offer clues into the load design in confined combustion chamber.

Figures 23(a)–(d) are the mass fractions of species in initial chamber during ejection. Figure 23(a) is the O_2 curves in the initial chamber during ejection. From the O_2 curves, we can see that O_2 mass fractions of four cases all decrease from 0.23 to 0 before ejection is finished. Additionally, the assumption rate of O_2 in initial chamber is different, the smallest ring-cavity volume has the fastest assumption rate. For the no ring-cavity case, the workout time of O_2 is $t = 0.21$ s, while for the 0.48 m^3 case $t = 0.7$ s. O_2 is closely related to the secondary-combustion process, so we can preliminarily conclude that adding ring-cavity volume could postpone the combustion process.

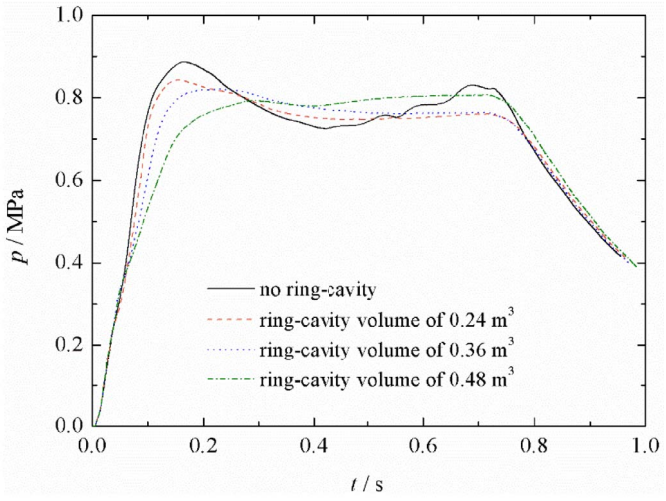

(a) Pressure curve

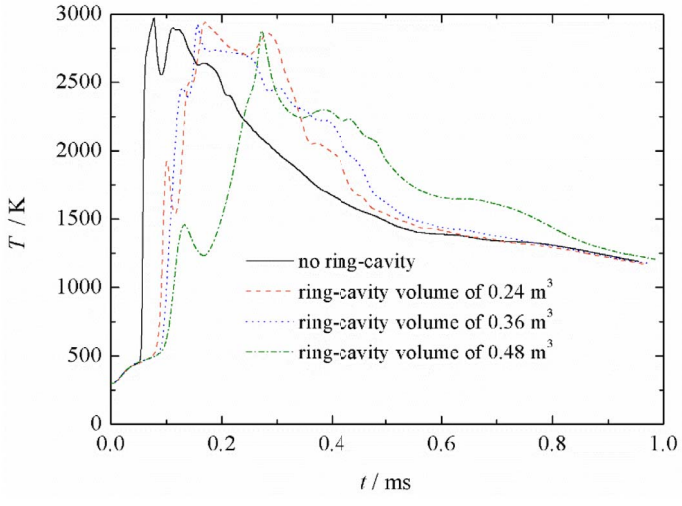

(b) Temperature curve

Figure 22. Load comparison in initial chamber.

Figures 23(b)–(e) are the reactant and product mass fraction curves in reactions of $CO + O_2 = CO_2$ and $H_2 + O_2 = H_2O$ during ejection. From the CO and H_2 mass fraction curves, we can see that in the four cases reactions increase slowly from the beginning to 0.25 s, then increase faster from 0.25 s to 0.75 s, and finally maintain stable values, which are 0.46 for CO and 0.042 for H_2, respectively. These two stable values are close to the mass fractions of nozzle inlet. Considering O_2 mass fraction variation during the ejection, we can conclude that the secondary-combustion has a close relationship to the reactant curves. At the beginning, CO and H_2 take part in the chemical reactions, so that reactant curves increase slowly. As the O_2 is working out, the mass fraction curves of reactants increase faster. Additionally, the larger ring-cavity volume, the faster the increase in mass fraction of reactant, which further proves that adding larger ring-cavity volume could postpone the combustion process.

Product curves of CO_2 and H_2O in Figures 23(c) and (e) increase from the beginning to $t = 0.2$ s, then decrease from $t = 0.2$ s to $t = 0.75$ s, and finally keep stable values, which are 0.04 for

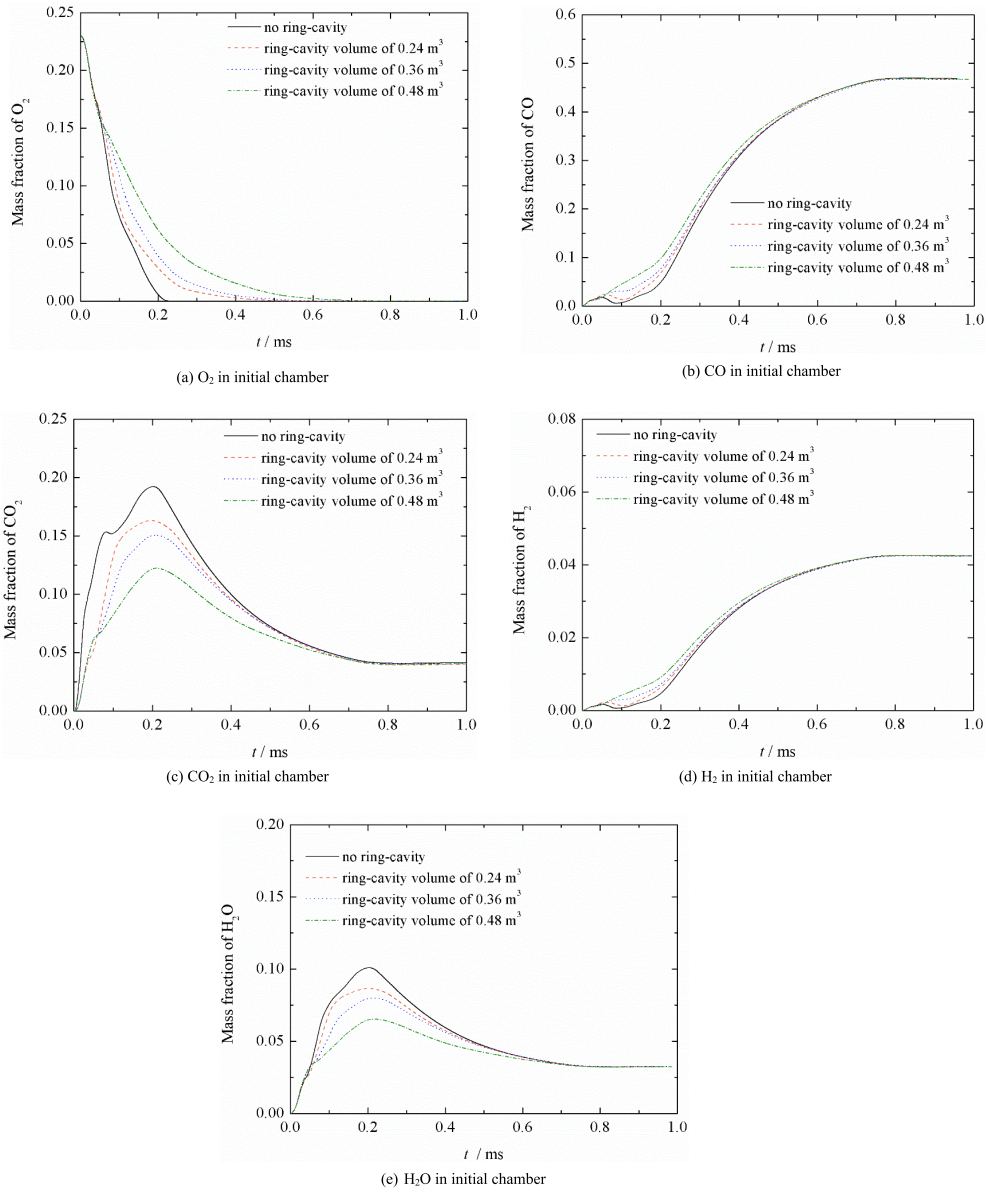

Figure 23. Mass fractions of species in initial chamber.

CO_2 and 0.03 for H_2O, respectively. The increase of CO_2 and H_2O at the initial time could be attributed to two aspects: first, the CO_2 and H_2O from nozzle of gas generator is ejected into initial chamber during the whole ejection process; second, secondary-combustion produces combustion products in reactions of $CO + O_2 = CO_2$ and $H_2 + O_2 = H_2O$. Influenced by the two factors, product curves of CO_2 and H_2O increase from beginning time to $t = 0.2$ s. After $t = 0.2$ s, O_2 in initial chamber is worked out gradually. CO_2 and H_2O in initial chamber mainly come from the nozzle outlet of gas generator. The low mass fraction species, such as CO_2 and H_2O, are diluted by other high mass fraction species. The curves of CO_2 and H_2O begin to go down.

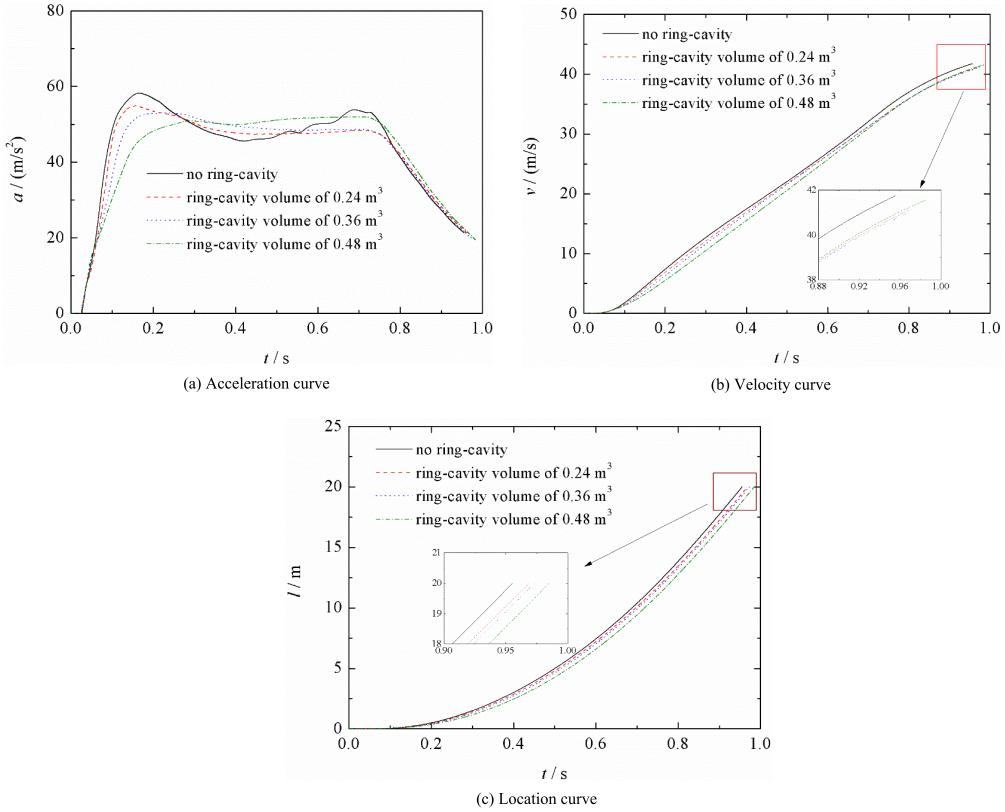

Figure 24. Interior ballistic curves with different ring-cavity volume.

Finally, the mass fraction of species maintains a dynamic balance, which shows a stable value in species mass fraction curves.

4.4. *Discussion of interior ballistics*

Figures 24(a)–(c) show interior ballistic curves with four different ring-cavity volumes. The velocities and locations of rail cover with ring-cavity cases behave more similarly to the no ring-cavity case in Figures 24(b), (c). However, the peaks and valleys of acceleration have significant differences in Figure 24(a).

On account of the aircraft sitting on the rail cover, we use interior ballistic parameters of rail cover to present the aircraft interior trajectory. Acceleration of rail cover is presented in Figure 24(a). The curves with ring-cavity are qualitatively different from the no ring-cavity case. These plots reveal that larger ring-cavity structure could reduce the first acceleration peak and smooth acceleration plot during ejection. In no ring-cavity case, the first acceleration peak is 59 m/s^2 at $t = 0.18$ s, while the case with ring-cavity volume of 0.48 m^3 is 50 m/s^2 at $t = 0.3$ s. The tendency of secondary accelerations in the four cases is that the peaks decline while ring-cavity volume changes from 0 to 0.36 m^3, and then increase in the 0.48 m^3 ring-cavity volume case. From the four acceleration curves, we can see that the acceleration of 0.48 m^3 case is smoother than that of any other curves.

Figure 24(b) presents the velocity plots comparison during ejection in the four cases. From the velocity curves, we can see that adding ring-cavity volume can reduce the out-tube-velocity.

For no ring-cavity case, the out-tube-velocity is 41.9 m/s; while for the 0.36 m^3 ring-cavity volume case is 41 m/s. With the ring-cavity volume increasing from 0.36 m^3 to 0.48 m^3, the out-tube-velocity is kept at 41.9 m/s nearby. Figure 24(c) depicts the location of rail cover of four cases during ejection. From the location curves, we can see that adding ring-cavity volume can delay the out-tube-time.

5. Conclusions

(1) This work focused on the effect of ring-cavity on secondary-combustion and interior ballistic stabilization with low-temperature solid propellant in gas ejection. Numerical simulation analyses are based on the good agreement between numerical pressure and temperature loads and experimental data in published literature. We analysed the development and propagation of secondary-combustion in initial chamber at founding time with four different ring-cavity structures, and their effects on the loads and species in the initial chamber and interior ballistics during ejection.

(2) Streamlines and temperature fields revealed the development and propagation of secondary-combustion high-temperature zone in initial chamber. The secondary-combustion process at founding time can be divided into three stages: a pair of spherical high-temperature zone, high-temperature zone with skirt touching walls and high-temperature zone reverses from rail cover. Larger volume ring-cavity can accelerate the axial and radial secondary-combustion high-temperature zone velocity on the ring-cavity cross-section.

(3) The expressions of two pressure peak values varying with ring-cavity volume in initial chamber are presented. Load and species characteristics are closely related with the volume of ring-cavity. Larger volume of ring-cavity can reduce the pressure peaks and postpone temperature peak time. However, there is little influence on the temperature peak during ejection.

(5) By monitoring the species mass fraction variations in initial chamber, we can conclude that larger ring-cavity volume can slow the consumption of O_2 while ring-cavity volumes change from zero to 0.48 m^3, which proves that adding larger ring-cavity volume can postpone the combustion process.

(6) Comparing four different ring-cavity interior ballistic plots, there are clear distinctions between ring-cavity cases and no ring-cavity cases. The acceleration plots show that adding ring-cavity in the initial chamber could decrease the acceleration peaks and increase the acceleration valleys, and further smooth the acceleration curves. In four cases, adding 0.48 m^3 ring-cavity volume can get the smoothest acceleration curve. For the velocity and location of rail cover during ejection, adding ring-cavity can reduce the velocity of out tube and delay the out-tube-time.

The development of ring-cavity is meant to extend the secondary-combustion controlling strategy and better improve the working performance in confined space.

Acknowledgments

The authors would like to acknowledge the Natural Science Foundation of the colleges and universities in Anhui Province (KJ2020A0241, KJ2017A062) for providing the fund for simulations.

References

[1] E. A. Salgansky, N. A. Lutsenko, V. A. Levin, L. S. Yanovskiy, "Modeling of solid fuel gasification in combined charge of low-temperature gas generator for high-speed ramjet engine", *Aerosp. Sci. Technol.* **84** (2019), p. 31-36.

[2] Y. J. Shao, W. Zhang, Q. H. Gao, G. Tian, Z. W. Yang, A. B. Ming, "Dynamic modeling of exergy efficiency and parameters optimization for gas ejection system", *Appl. Therm. Eng.* **146** (2019), p. 931-942.

[3] P. Baiocco, G. Ramusatm, A. Sirbi, T. Bouilly, F. Lavelle, T. Cardone, H. Fischer, S. Appel, "System driven technology selection for future European launch systems", *Acta Astronaut.* **107** (2015), p. 301-316.
[4] Y. Wu, X. Qu, "Obstacle avoidance and path planning for carrier aircraft launching", *Chin. J. Aeronaut.* **28** (2015), p. 659-703.
[5] J. Ren, F. B. Yang, D. W. Ma, G. G. Le, J. L. Zhong, "Pneumatic performance study of a high pressure ejection device based on real specific energy and specific enthalpy", *Entropy* **19** (2014), p. 1593-1596.
[6] R. Pucclo, F. Maggl, G. Columbo, "Low-temperature gas generator propellants", in *XXI Italian Association of Aeronautics and Astronautics (AIDAA) Congress and 3rd International Conference of the European Aerospace Societies (CEAS), 11 October 2011* (Venice, Italy), 2011, p. 24-28.
[7] A. Vorozhtsov, S. Bondarchuk, A. Salko, O. Kondratova, "Mathematical simulation of airbag inflation by low-temperature gas generator products", *Propellant. Explos. Pyrotech.* **25** (2000), p. 220-223.
[8] V. Shandakov, V. Puzanov, V. Komarov, V. Borachkin, "The method of low-temperature generating in solid gas generators", *Fiz. Goreniya I Vzryva* **4** (1999), no. 4, p. 75-78.
[9] V. A. Levin, N. A. Lutsenko, E. A. Salgansky, L. S. Yanovskiy, "A model of solid-fuel gasification in the combined charge of a low-temperature gas generator of a flying vehicle", *Doklay Phys.* **63** (2018), p. 375-379.
[10] V. E. Zarko, L. K. Gusachenko, *Simulation of Energetic Materials Combustion*, Russian Academy of Sciences Novosibirsk Inst of Chemical Kinetics and Combustion, Saint Petersburg, Russia, 2000, http://dx.doi.org/10.1002/ijc.2910600627.
[11] A. I. Atwood, T. L. Boggs, P. O. Curran, T. P. Parr, D. M. Hanson-Parr, C. F. Price, "Burning rate of solid propellant ingredients, Part 1: Pressure and initial temperature effects", *J. Propul. Power* **15** (1999), p. 740-747.
[12] V. A. Strunin, L. I. Nikolaeva, "Influence of additives on the characteristics of the combustion of layered systems imitating composite propellants", *Combust. Explos. Shockwaves* **11** (2017), p. 419-428.
[13] D. Claresta, B. Brian, "On the combustion of heterogeneous AP/HTPB composite propellants: A review", *Fuel* **254** (2019), p. 1-15.
[14] J. U. Schlüter, "Static control of combustion oscillations by coaxial flows: a large-eddy-simulations investigation", *J. Propul. Power* **20** (2004), p. 460-467.
[15] B. Wang, Z. M. Rao, Q. F. Xie, P. Wlański, G. Rarata, "Brief review on passive and active methods for explosion and detonation suppression in tubes and galleries", *J. Loss Prev. Process Ind.* **49** (2017), p. 280-290.
[16] R. C. Steele, L. H. Cowell, S. M. Cannon, C. E. Smith, "Passive control of combustion instability in lean premixed combustors", *J. Eng. Gas Turbines Power* **122** (2000), p. 414-419.
[17] J. D. Eldredge, A. P. Dowling, "The absorption of axial acoustic waves by a perforated liner with bias flow", *J. Fluid Mech.* **485** (2003), p. 307-335.
[18] D. L. Gysling, G. S. Copeland, D. C. McCormck, W. M. Proscia, "Combustion system damping augmentation with Helmholtz resonators", *J. Eng. Gas Turbines Power* **122** (2000), p. 269-274.
[19] J. C. Oefelein, V. Yang, "Comprehensive review of liquid-propellant combustion instabilities in F-1 engines", *J. Propul. Power* **9** (1993), p. 657-677.
[20] S. Meng, H. Zhou, K. Cen, "Application of perforated plate in passive control of the nonpremixed swirl combustion instability under acoustic excitation", *J. Eng. Gas Turbines Power* **141** (2019), no. 9, p. 1-12.
[21] H. Zhou, Z. H. Liu, H. Fang, C. F. Tao, "Attenuation effects of perforated plates with heterogeneously distributed holes on combustion instability in a spray flame combustor", *J. Mech. Sci. Technol.* **34** (2020), no. 11, p. 4865-4875.
[22] H. Zhou, Z. H. U. Liu, C. F. Tao, M. X. Zhou, "Mitigating self-excited thermoacoustic oscillations in a liquid fuel combustor using dual perforated plates", *J. Acoust. Soc. Am.* **148** (2020), no. 3, p. 1755-1766.
[23] N. Tran, S. Ducruix, T. Schuller, "Passive control of the inlet acoustic boundary of a swirled burner at high amplitude combustion instabilities", *J. Eng. Gas Turbines Power* **131** (2009), article no. 051502.
[24] A. Scarpato, N. Tran, S. Ducruix, T. Schuller, "Modeling the damping properties of perforated screens traversed by a bias flow and backed by a cavity at low Strouhal number", *J. Sound Vib.* **331** (2012), p. 276-290.
[25] A. Scarpato, S. Ducruix, T. Schuller, "A comparison of the damping properties of perforated plates backed by a cavity operating at low and high Strouhal numbers", *C. R. Mec.* **341** (2013), p. 161-170.
[26] J. P. V. Doormaal, G. D. Raithby, "Enhancement of the simple method for predicting incompressible fluid flows", *Numer. Heat Transf.* **7** (1984), p. 147-163.
[27] S. W. Kim, T. J. Benson, "Calculation of a circular jet in crossflow with a multiple-time-scale turbulence model", *Int. J. Heat Mass Transf.* **35** (1992), p. 2357-2365.
[28] P. Sathiah, E. Komen, D. Roekaerts, "The role of CFD combustion modeling in hydrogen safety management-Part I: Validation based on small scale experiments", *Nucl. Eng. Des.* **248** (2012), p. 93-107.
[29] Z. Han, R. D. Reitz, "Turbulence modeling of internal combustion engines using RNG $k-\varepsilon$ models", *Combust. Sci. Technol.* **106** (1995), p. 267-295.
[30] Chemical Equilibrium Applications (CEA) software: https://federallabs.org/technology/chemical-equilibrium-applications-cea.

[31] X. L. Hu, G. G. Le, D. W. Ma, J. Ren, X. H. Zhou, "The influence of annular cavity on secondary combustion of gas-ejection initial cavity", *Acta Armamentarii* **36** (2015), no. 6, p. 1024-1032.
[32] H. J. Chen, X. Zhao, Y. Zhao, L. Gao, "Influence of structural parameters of diversion cone on smooth effect of gas ejection bottom pressure impact", *J. Propul. Technol.* **40** (2019), no. 11, p. 2444-2453.
[33] H. H. Xiao, D. Makarov, J. H. Sun, V. Molkov, "Experimental and numerical investigation of premixed flame propagation with distorted tulip shape in a closed duct", *Combust. Flame* **159** (2012), p. 1523-1538.
[34] H. H. Xiao, R. W. Houim, E. S. Oran, "Formation and evolution of distorted tulip flames", *Combust. Flame* **162** (2015), p. 4084-4101.
[35] J. D. Ott, E. S. Oran, J. D. Anderson, "A mechanism for flame acceleration in narrow tubes", *AIAA J.* **41** (2003), p. 1391-1396.
[36] V. N. Kurdyumov, M. Matalon, "Flame acceleration in long narrow open channels", *Proc. Combust. Inst.* **34** (2013), p. 865-872.